Inorganic Chemistry

Article

Crystal Structure and Physical Properties of the Cage Compound $Hf_2B_{2-2\delta}Ir_{5+\delta}$

Olga Sichevych, Sever Flipo, Alim Ormeci, Matej Bobnar, Lev Akselrud, Yurii Prots, Ulrich Burkhardt, Roman Gumeniuk, Andreas Leithe-Jasper,* and Yuri Grin

Read Online

ACCESS | Metrics & More | Article Recommendations | Supporting Information

ABSTRACT: $Hf_2B_{2-2\delta}Ir_{5+\delta}$ crystallizes with a new type of structure: space group *Pbam*, a = 5.6300(3) Å, b = 11.2599(5) Å, and c = 3.8328(2) Å. Nearly 5% of the boron pairs are randomly replaced by single iridium atoms ($Ir_{5+\delta}B_{2-2\delta}$). From an analysis of the chemical bonding, the crystal structure can be understood as a three-dimensional framework stabilized by covalent two-atom B−B and Ir−Ir as well as three-atom Ir−Ir−B and Ir−Ir−Ir interactions. The hafnium atoms center 14-atom cavities and transfer a significant amount of charge to the polyanionic boron−iridium framework. This refractory boride displays moderate hardness and is a Pauli paramagnet with metallic electrical resistivity, Seebeck coefficient, and thermal conductivity. The metallic character of this system is also confirmed by electronic structure calculations revealing 5.8 states eV^{-1} fu^{-1} at the Fermi level. $Zr_2B_{2-2\delta}Ir_{5+\delta}$ is found to be isotypic with $Hf_2B_{2-2\delta}Ir_{5+\delta}$, and both form a continuous solid solution.
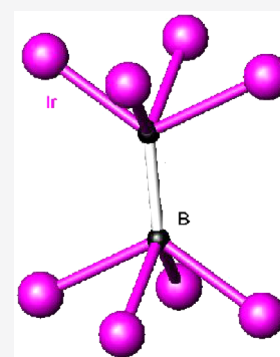
1. INTRODUCTION

The structural chemistry of metal borides displays a vast diversity.[1] The inherent electron deficiency of boron can be seen as the main ingredient necessary for the high structural complexity.[2] Depending on the metal to boron ratio, the formation of multicenter B−B bonds gives rise to the evolution of boron-based framework structures with increasing dimensionality.[3−5] The boride's crystal structures are characterized by strong covalent boron−boron and metal−boron bonds.[6,7]

This gives rise to interesting structure−properties relationships which have been topic of the solid-state sciences for decades. The inherent hardness,[8] wear resistance, and chemical inertness[9] of borides belong to the group of phenomena which have been observed and studied from the very beginning of research on this class of materials.[6] Applications such as abrasives, cermet-based specialty cutting tools,[10−13] or tough alloy surface coatings[14] take advantage of these properties.

Other technologically demanding developments are ultra-high-temperature boride-based ceramics[15] and ceramic coatings[16] as well as the field of superhard materials, where alternatives to diamond and cubic boron nitride are sought. The increasing surge in theoretical and experimental research activities focusing on ReB_2[17,18] and OsB_2[19] also raised significant interest in other transition-metal polyborides.[20−25] The high electron concentration of heavy 5d transition metals, leading to high elastic moduli, in combination with the highly directional covalent bonds is important for the physical properties of this category of superhard borides. For that reason, research has currently intensified on elucidating and understanding the influence of boron incorporation in heavy transition metals.

HfB_2 with a hexagonal AlB_2 type of structure and a high melting point of 3400 °C also belongs to this family of refractory diborides.[26,27] It has found its way into nuclear applications as neutron absorber materials[28] and high-temperature ceramic composites.[29,30]

Also, platinum metals and their interaction with boron have been the targets of investigation,[31−35] which have been directed toward an understanding of their distinct structural chemistry and/or exploration of their mechanical properties. The binary iridium boron system has been studied thoroughly,[36,37] and recent attention is mainly due to joint theoretical and experimental classification of some iridium borides as potentially superhard materials.[38−40]

The structural diversity significantly increases for the numerous families of ternary and higher multicomponent transition-metal-based borides.[4,41−44] Taking alone the large structural variety of noble-metal-based ternary and higher boride systems and combining them with all the possibilities of a diverse interplay between physical properties, such as superconductivity and magnetism, the considerable interest
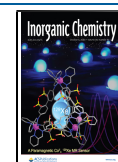
in explorative studies can be easily motivated and explained.[45−52]

Given the recent interest in the platinum-group-metal superalloys, related intermetallic compounds for high-temperature oxidation-resistant structural applications,[53−59,65] and the concomitant need for brazing alloy systems, a detailed knowledge of ternary Ir-based phase diagrams is desirable. Joining small casted parts of such alloys helps to minimize size-dependent casting defects; transient liquid phase (TLP) bonding,[60] a technology developed for joining and repairing Ni-based superalloys,[61,62] could be an obvious choice. To achieve this, a melting-point depressant is placed between the two mating surfaces, which is typically a boride-based eutectic, where the highly diffusive boron reduces the melting point, due to low-lying eutectic formation. As an example, a eutectic is formed in the Ir-rich part (37.5 atom % boron) of the binary Ir−B system at 1259 °C.[22,35] One could therefore envision employing boron as a melting-point depressant also in Ir−Zr−Hf-based superalloys,[63−65] in a way similar to Ni-based superalloys joining technologies. However, as is known from numerous studies when boron is used as a melting point depressant, it is very difficult to avoid the precipitation of brittle borides.[66,67] They have a detrimental effect on the mechanical properties as well as on the corrosion resistance. This is a strong motivation for investigating the occurrence of Ir−Zr/Hf-based borides, their crystal structures, and thus the structure−properties relationships in these materials.

The isothermal sections of the phase diagrams of Zr−Ir−B and Hf−Ir−B ternary systems at 1100 °C were investigated some time ago.[68] Three ternary borides—hexagonal $ZrIr_3B_4$ ($HfIr_3B_4$ type) (also reported later as a $ZrIr_3B_{3.76}$ composition[69]) as well as $\sim ZrIr_3B_2$, and $\sim ZrIr_5B_4$ with unknown structures—were detected in the Zr−Ir−B system. Additionally, cubic Zr_2Ir_6B (K_2PtCl_6 type) was reported later to exist.[70] However, five compounds have been reported to occur in the Hf−Ir−B system: tetragonal $Hf_3Ir_5B_2$ ($Ti_3Co_5B_3$ type[71]), hexagonal $HfIr_3B_4$ (its own type of structure[69]), $HfIr_3B_{0.45}$ (structure type $CaTiO_3$[68]), and $\sim HfIr_3B_2$ and $\sim HfIr_5B_4$ with unknown structures.

In light of the aforementioned interest in Ir-rich ternary borides, we started to search for these last two compounds, which yielded as a byproduct the ternary phase $Hf_2B_{2−2\delta}Ir_{5+\delta}$ with a new type of crystal structure and its $Hf_{2−x}Zr_xB_{2−2\delta}Ir_{5+\delta}$ solid solution.

2. EXPERIMENTAL SECTION

Samples with the nominal compositions $ZrIr_{2.7}B_{1.6}$, $HfIr_{2.7}B_{1.6}$, and $Hf_2Ir_5B_2$ were prepared from Zr powder (Alfa-Aesar, 98.5% metals base, with Hf 2% nominal content), Zr crystal bar (Haines & Maassen, 99.9% metals base, with 280(20) ppm of Hf as analyzed by ICP-OES), Hf powder (Chempur, 99.8% metals base, with 2.9(1)% Zr as analyzed by ICP-OES), Hf pellets (Haines & Maassen, 99.9% metals base, with 0.11(1)% Zr as analyzed by ICP-OES), Ir powder (Chempur, 99.9%), and B crystalline powder (Chempur, 99.99%). First, B and Ir powders were pressed into a pellet, placed in a ZrO_2 crucible, enclosed in an evacuated Ta tube, and annealed at 1270 K for 4 days. This led to (i) homogeneous Ir−B precursors with rather low melting points (see the Introduction) and (ii) suppression of the competing formation of HfB_2 in the second step of synthesis. Then, this pellet was arc-melted with Hf pieces under an Ar atmosphere on a water-cooled copper hearth (mass losses <2%). Further heat treatment was performed between 1470 and 1570 K for several weeks. All described handlings and procedures were carried out in Ar-filled gloveboxes (MBraun, $p(O_2/H_2O) \leq 1$ ppm).

The obtained samples were characterized by powder X-ray diffraction (PXRD) with a Huber G670 imaging plate Guinier camera and Cu $K\alpha1$ radiation ($\lambda = 1.54056$ Å, using a curved germanium (111) monochromator). Phase analysis and indexing have been carried out using the WinXPow program package.[72] High-resolution powder XRD was performed at the BM20 beamline of the European Synchrotron Radiation Facility (Grenoble, France) ($\lambda = 0.45920$ Å) on powder enclosed in a quartz capillary with an outer diameter of 0.3 mm. The images collected on a Pilatus 100K detector[73] were integrated with the PYFAI library.[74] Indexing of PXRD patterns and Rietveld refinement of the crystal structure were performed using the WinCSD software.[75]

Single crystals were mechanically extracted from an arc-melted and annealed sample made by using Hf powder containing a considerable amount of Zr (see above) as a Hf source with the composition $HfIr_{2.7}B_{1.6}$. For $Hf_2Ir_5B_2$ and $Zr_2Ir_5B_2$, attempts to isolate single crystals of sufficient quality failed. Single-crystal XRD was performed on a Rigaku AFC7 diffraction system equipped with a Saturn 724+ CCD Detector (Mo $K\alpha$ radiation, $\lambda = 0.710730$ Å, graphite monochromator). The crystal structure solution and refinement were performed using the WinCSD program package.[75]

Differential scanning calorimetry has been performed by means of a DSC NETZSCH 404 C instrument in the temperature range 300−1870 K. Both $Zr_2B_{2−2\delta}Ir_{5+\delta}$ and $Hf_2B_{2−2\delta}Ir_{5+\delta}$ reveal no thermal effects either during heating or upon cooling, suggesting that the studied samples do not melt in the mentioned temperature range.

For microstructural studies, small pieces of the new ternary boride were embedded in a conductive resin, polished, and ground. The obtained polished surface was investigated using a Zeiss Axioplan 2 light-optical microscope and a Jeol JSM-7800F scanning electron microscope. The chemical composition was analyzed by means of energy dispersive X-ray spectroscopy (EDXS, Quantax 400 EDXS system, Bruker) and wavelength dispersive X-ray spectroscopy (WDXS, SX 100 setup, Cameca) with Ir metal and HfB_2 as reference materials. WDXS measurements on a sample synthesized from Hf metal pellets (see above) confirmed the Hf:Ir ratio to be very close to 2:5, while the total composition (i.e., $Hf_{1.9(1)}Ir_{4.9(1)}B_{2.0(3)}$) deviated slightly from the nominal composition due to the inaccuracy of the estimation of the small (i.e., 1.6 mass %) boron amount.

The magnetic susceptibility was measured in the temperature range 1.8−400 K in external fields between 0.1 and 7 T using a SQUID magnetometer (MPMS-XL7, Quantum Design). The electrical resistivity, Seebeck coefficient, and thermal conductivity were simultaneously measured using the TTO option of a Physical Property Measurement System (PPMS, Quantum Design).

Electronic structure calculation and bonding analysis for $Hf_2B_2Ir_5$ were carried out using the experimental values of the lattice parameters and the atomic coordinates for the ordered model without multiple substitution ($\delta = 0$). The electronic density of states for $Hf_2B_2Ir_5$ was obtained within the local density approximation (LDA) to the density functional theory (DFT). Calculations were performed by using the all-electron, full-potential local orbital method (FPLO, version 9.01-35)[76] by employing the exchange-correlation potential of Perdew and Wang.[77] The first Brillouin zone was sampled by a mesh of $20 \times 20 \times 20$ (8000) k points.

Chemical bonding analysis in position space was performed within the approach of combined topological analysis of electron density (ED) and electron localizability indicator (ELI). The former type of analysis forms the basis of the quantum theory of atoms in molecules (QTAIM).[78] ELI was calculated in the ELI-D representation[79−81] by a module implemented in the FPLO package.[82] Topological analyses of the ED and the ELI-D were carried out by the program DGrid.[83] To obtain the atomic charges from ED and bond populations for bonding and lone-pair basins from ELI-D, both the ED and the ELID were integrated within the space regions (basins), bounded by zero-flux surfaces in the according gradient field. The procedure proposed follows the QTAIM.[78] A combined analysis of ED and ELI-D allows obtaining basic information for the description of the bonding situation in solids, in particular for intermetallic compounds.

3. RESULTS AND DISCUSSION

3.1. Crystal Structure. Since single crystals were originally extracted from samples made from Hf powder containing considerable amounts of Zr (see the Experimental Section), the crystallographic details on the single-crystal diffraction performed on $Hf_{2-x}B_{2-2\delta}Zr_xIr_{5+\delta}$ ($x \approx 0.5$, $\delta \approx 0.05$) are given in Table 1. An analysis of the extinction conditions indicated

Table 1. Crystallographic Data for $Hf_{2-x}B_{2-2\delta}Zr_xIr_{5+\delta}$ ($x \approx 0.5$, $\delta \approx 0.05$)) and $Hf_2B_{2-2\delta}Ir_{5+\delta}$ (Space Group *Pbam*, Z = 2)

	$Hf_{2-x}B_{2-2\delta}Zr_xIr_{5+\delta}$ ($x \approx 0.5$, $\delta \approx 0.05$)	$Hf_2B_{2-2\delta}Ir_{5+\delta}$
diffraction material	single crystal	powder
crystal shape	irregularly shaped	
cryst size (mm³)	0.015 × 0.030 × 0.040	
diffraction system	Rigaku AFC-7	BM20
radiation, λ (Å)	Mo Kα, 0.710730	synchrotron, 0.45920
$\sin \theta/\lambda_{max}$	0.775	0.766
unit cell params (powder data)		
a (Å)	5.6290(9)	5.6300(3)
b (Å)	11.270(2)	11.2599(5)
c (Å)	3.8444(5)	3.8328(2)
V (Å³)	243.9(1)	242.97(3)
calcd density ρ (g cm⁻³)	17.79	18.26
h, k, l ranges	$-5 \leq h \leq 8$	$0 \leq h \leq 8$
	$-17 \leq k \leq 15$	$0 \leq k \leq 17$
	$-4 \leq l \leq 5$	$0 \leq l \leq 5$
abs cor	numerical	
abs coeff (mm⁻¹)	180.29	65.51
$N(hkl)$ measd	1592	518
$N(hkl)$ obsd	461	
observation criterion	$F(hkl) \geq 4\sigma(F)$	
no. of refined params	34	17
R_F, R_I, R_W, R_P	0.037; 0.040	0.045, 0.068
residual peaks (e Å⁻³)	−4.19/5.68	

the two possible space groups *Pba*2 (No. 32) and *Pbam* (No. 55). Starting with the centrosymmetric space group, we applied direct methods to find the positions of heavier Hf and

Ir atoms. Further differential Fourier calculations allowed localization of boron atoms. During the refinement the displacement parameter B_{eq} for Hf was found to be twice as large as that of Ir atoms. Thus, this position was assumed to be occupied by a statistical mixture of Hf and Zr (cf. the composition of the initial hafnium powder in the Experimental Section). The content of Zr in this position is higher in comparison to the initial powder, indicating a special suitability of the atomic environment for occupancy by zirconium. At this stage, the residual value was relatively low (0.042). Nevertheless, an analysis of the difference electron density reveals an additional peak at the 2d site (0,1/2,1/2). Because of spatial collision with the boron atoms ($d = 0.91$ Å), it was assumed that this position is occupied by iridium, i.e. the random replacement of ca. 5% of boron pairs by single iridium atoms, as this was already found in $Mg_2Rh_{1-x}B_{6+2x}$.[98] This minor substitution significantly reduced the residual value to 0.037. The final values of atomic coordinates and displacement parameters for $Hf_{2-x}B_{2-2\delta}Zr_xIr_{5+\delta}$ ($x \approx 0.5$, $\delta \approx 0.05$) are given in Table 2, and the anisotropic displacement parameters are collected in Table 3.
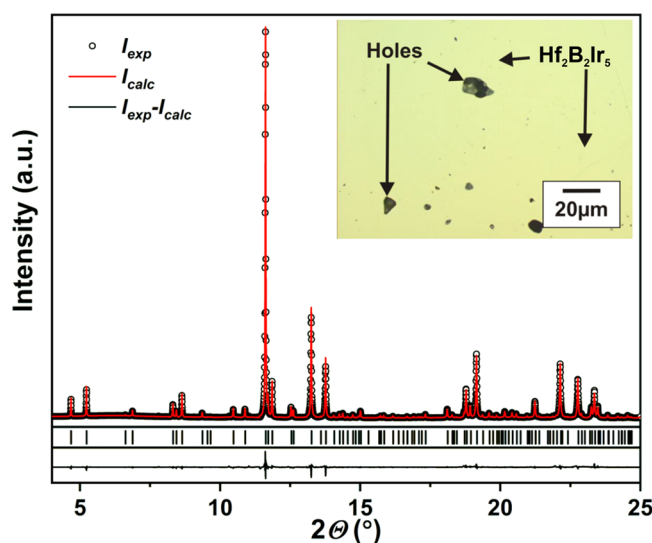
Table 3. Anisotropic Displacement Parameters for $Hf_{2-x}B_{2-2\delta}Zr_xIr_{5+\delta}$ ($x \approx 0.5$, $\delta \approx 0.05$)

atom	B_{11}	B_{22}	B_{33}	B_{12}[a]
Hf	0.54(5)	0.49(4)	0.65(4)	−0.06(3)
Ir1	0.71(5)	0.39(4)	0.54(4)	0.02(4)
Ir2	0.34(3)	0.30(3)	0.37(3)	−0.05(2)
Ir3	0.44(4)	0.37(3)	0.47(3)	0.08(3)

[a]$B_{13} = B_{23} = 0$ for all Hf and Ir positions.

Additionally, a close to single-phase ternary sample of $Hf_2B_{2-2\delta}Ir_{5+\delta}$ (inset to Figure 1) was prepared from Hf metal with significantly reduced Zr content (see the Experimental Section) and characterized with high-resolution synchrotron (HRS) XRD at BM20 at ESRF.

As the initial model for the Rietveld structure refinement, the atomic parameters from $Hf_{2-x}B_{2-2\delta}Zr_xIr_{5+\delta}$ ($x \approx 0.5$, $\delta \approx 0.05$) (Table 2) were used. The refinement converged with low reliability factors (Table 1) and physically reasonable displace-

Table 2. Atomic Coordinates and Occupational and Displacement Parameters for $Hf_{2-x}B_{2-2\delta}Zr_xIr_{5+\delta}$ ($x \approx 0.5$, $\delta \approx 0.05$) and $Hf_2B_{2-2\delta}Ir_{5+\delta}$

atom	site	occ	x	y	z	B_{eq}[a]/B_{iso} (Å²)
			$Hf_{2-x}B_{2-2\delta}Zr_xIr_{5+\delta}$ ($x \approx 0.5$, $\delta \approx 0.05$)			
M	4g	0.76(1) Hf + 0.24(1) Zr	0.2871(2)	0.1128(1)	0	0.56(3)
Ir1	2b	1	0	0	1/2	0.55(3)
Ir2	4h	1	0.0340(2)	0.24666(7)	1/2	0.33(2)
Ir3	4g	1	0.7797(2)	0.13189(7)	0	0.42(2)
Ir4	2d	0.05(1) Ir	0	1/2	1/2	0.6(3)
B	4h	0.949(6) B	0.612(5)	0.058(3)	1/2	0.6(4)
			$Hf_2B_{2-2\delta}Ir_{5+\delta}$			
Hf	4g	1	0.290(1)[b]	0.1128(6)	0	0.7(2)
Ir1	2b	1	0	0	1/2	0.8(2)
Ir2	4h	1	0.036(2)	0.2462(5)	1/2	0.8(2)
Ir3	4g	1	0.781(1)	0.1319(6)	0	0.7(2)
Ir4	2d	0.06 Ir	0	1/2	1/2	1.3(4)
B	4h	0.94(2) B	0.580(30)	0.088(15)	1/2	1.2(4)

[a]$B_{eq} = 1/3[B_{11}a^{*2}a^2 + ... + 2B_{23}b^*c^*bc \cos \alpha]$ for M and Ir1−Ir3 in $Hf_{2-x}Zr_xIr_{5+\delta}B_{2-2\delta}$ ($x \approx 0.5$, $\delta \approx 0.05$), B_{iso} for all other atoms. [b]Estimated standard deviations are calculated by the method of Bérar and Lellan.[99]

Figure 1. Powder XRD pattern for $Hf_2B_{2-2\delta}Ir_{5+\delta}$ (red, calculated profile; black circles, measured intensities; black tick marks, reflection positions; black line in the bottom panel, difference intensity curve). Inset: microstructure of an annealed sample.

ments for all atoms (Table 2). Whereas from the laboratory X-ray powder diffraction data the additional position of Ir cannot be reliably refined, the high-resolution synchrotron data clearly confirm this crystallographic disorder. The experimental, calculated, and differential diffraction intensities for $Hf_2B_{2-2\delta}Ir_{5+\delta}$ are shown in Figure 1. The crystal structures of both $Hf_{2-x}B_{2-2\delta}Zr_xIr_{5+\delta}$ ($x \approx 0.5$, $\delta \approx 0.05$) and $Hf_2B_{2-2\delta}Ir_{5+\delta}$ reveal a unique atomic architecture and thus have to be considered as a new structure type.

The indexing of the HRS XRD pattern as well as the comparison of the theoretically calculated and experimentally observed intensities also confirmed the $Hf_2B_{2-2\delta}Ir_{5+\delta}$ structure type for $Zr_2B_{2-2\delta}Ir_{5+\delta}$ ($a = 5.6290(2)$ Å, $b = 11.2697(3)$ Å, $c = 3.8444(1)$ Å). However, the presence of numerous impurity phases (e.g., $ZrIr_4B_3$[69] and Zr_2Ir_6B[70]) did not allow us to refine the atomic coordinates and displacement parameters for this boride in a reasonable way.

The interatomic distances in the structure of $Hf_{2-x}B_{2-2\delta}Zr_xIr_{5+\delta}$ ($x \approx 0.5$, $\delta \approx 0.05$) are given in Table 4

Table 4. Selected Interatomic Distances (in Å) for $Hf_{2-x}B_{2-2\delta}Zr_xIr_{5+\delta}$ ($x \approx 0.5$, $\delta \approx 0.05$)

M^a−B (×4)	2.73(2)−2.78(2)	Ir3−B (×2)	2.30(2)
M^a−Ir (×10)	2.781(2)−2.878(1)	Ir3−Ir (×6)	2.7234(9)−2.7351(9)
M^a−Hf (×3)	3.494(2)−3.8444(6)	Ir3−Hf (×4)	2.781(1)−2.878(1)
M^a−Ir4 (×2)	2.5975(8)	Ir3−Ir4 (×2)	2.8952(7)
Ir1−B (×2)	2.28(3)	B−B	1.82(4)
Ir1−Ir (×6)	2.7281(7)−2.7864(4)	B−Ir (×4)	2.24(3)−2.30(2)
Ir1−Hf (×2)	2.8148(9)	B−Hf (×4)	2.72(2)−2.78(2)
Ir1−Ir4 (×2)	2.8145(4)	B−Ir4	0.91(3)
Ir2−B	2.24(3)		
Ir2−Ir (×7)	2.7234(9)−2.816(1)		
Ir2−Hf (×4)	2.829(1)−2.852(1)		
Ir2−Ir4	2.8616(8)		

^{a}M = $Hf_{0.76}Zr_{0.24}$.

(data for $Hf_2B_{2-2\delta}Ir_{5+\delta}$ can be found in Table S1 in the Supporting Information). The Hf−B, Hf−Hf, Hf−Ir, and B−B distances are close to or exceed the sums of atomic radii of the elements ($r_{Hf} = 1.56$ Å, $r_{Ir} = 1.36$ Å, and $r_B = 0.83$ Å[84]).

The coordination polyhedra of atoms in the structure of $Hf_2B_2Ir_5$ (ordered model without multiple substitution) are depicted in Figure 2 (top). Hafnium atoms are at the centers of
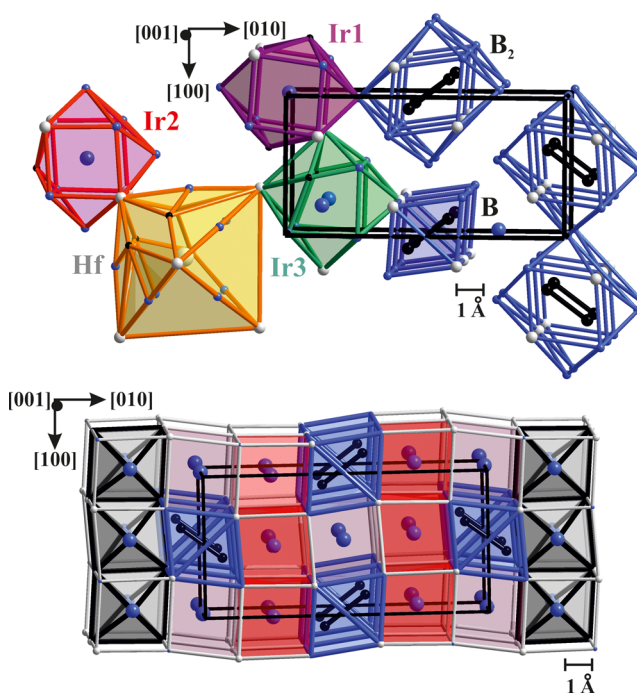

Figure 2. Crystal structure of $Hf_2B_2Ir_5$: (top) coordination polyhedra of atoms; (bottom) arrangement of the distorted cuboids [Ir1Hf$_4$Ir$_4$] (violet) and [Ir2Hf$_4$Ir$_4$] (red) and trigonal prisms [BHf$_4$Ir$_2$]. [□Ir1$_2$Ir3$_2$Hf$_2$] octahedra are shown as examples.

18-vertex [HfHf$_6$Ir$_8$B$_4$] polyhedra. This polyhedron can be understood as being formed on the basis of a [HfHf$_6$] octahedron. Ir1 and Ir2 are at the centers of distorted [Ir1Hf$_4$Ir$_6$B$_2$] and [Ir2Hf$_4$Ir$_7$B] cuboctahedra, thus having as the closest environment [Hf$_4$Ir$_4$] distorted cubes. Ir3 is located in a distorted [Ir3Hf$_4$Ir$_6$B$_2$] icosahedron typically occurring in the CeCo$_3$B$_2$ structure type.[85] Finally, the location of boron atoms can be geometrically described in different ways. They center trigonal prisms [BHf$_4$Ir3$_2$] which share their rectangular [Hf$_4$] face in pairs forming rhombic prisms. The B atoms are relatively close to each other ($d_{B-B} = 1.87(5)$ Å), forming B$_2$ dumbbells—a structural unit that is well-known in the chemistry of metal-rich intermetallic borides.[1,86] For $\delta \neq 0$, a single iridium atom is located in the center of such a cuboctahedron. The [B$_2$Hf$_4$Ir3$_4$] rhombic prisms are tetracapped by each two Ir1 and two Ir2 atoms, respectively, which result in [B$_2$Hf$_4$Ir3$_4$Ir1$_2$Ir2$_2$] entities (reminiscent of distorted cuboctahedra) forming slabs along the [001] direction and sharing their corners in the [100] direction (see Figure 2, top, and Figures S1 and S2). Such a description indicates a close crystallographic relationship of the $Hf_2B_{2-2\delta}Ir_{5+\delta}$ type with the homologous series of the borides based on α-Fe (W) and AlB$_2$ types.[1,87]

Structural similarities can be also found with the tetragonal Mo$_2$FeB$_2$ type.[88] In this crystal structure we observe tilted and distorted vertex-connected octahedra [□Fe$_4$Mo$_2$]. The voids

in this kind of 3D structure are distorted cuboctahedra filled with boron dumbbells (i.e., $[B_2Fe_8Mo_4]$) (Figure 3a,b). On an
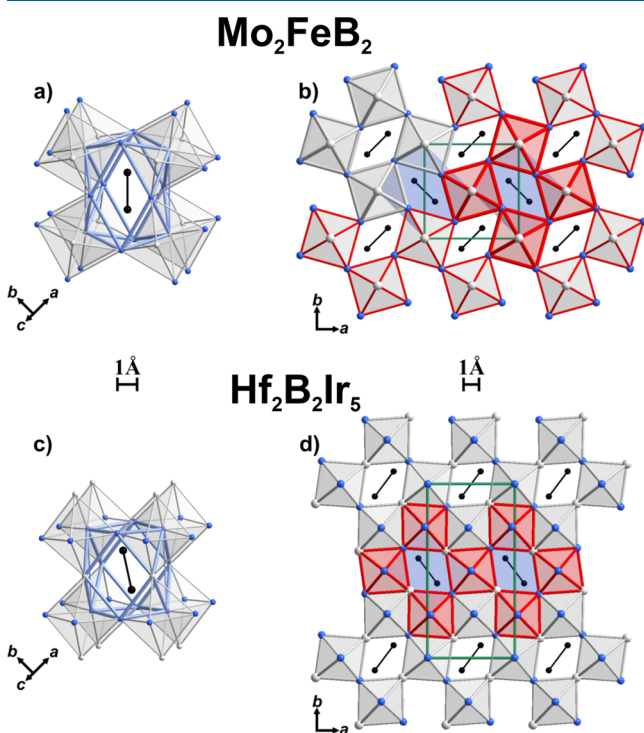

Figure 3. Two-dimensional intergrowth of filled cuboctahedral (square biantiprismatic) and empty octahedral segments in the crystal structures of Mo_2FeB_2 and $Hf_2B_2Ir_5$ (Hf, Mo, gray spheres; Ir, Fe, blue spheres; B, black spheres).

equal geometrical footing, one can recognize rhombic prismatic slabs along $[001]$ that can be decomposed into face-sharing trigonal prisms hosting the boron atoms. In $Hf_2B_{2-2\delta}Ir_{5+\delta}$, a related scenario is encountered. In order to discern this, one has to bear in mind that the slabs of Ir-centered cuboids can be also represented as $[\square Ir1_2Ir3_2Hf_2]$ and $[\square Ir2_2Ir3_2Hf_2]$ octahedra which share edges in the ab plane and are vertex-connected along $[001]$ (Figure 2, bottom, and Figures S1 and S2).

The tilting angle of the $[\square Ir_4Hf_2]$ octahedra in this structure (Figure 3c,d) is smaller than those of $[\square Fe_4Mo_2]$ in the Mo_2FeB_2 type (Figure 3a). However, in contrast to Mo_2FeB_2, in $Hf_2B_2Ir_5$ the unit cell geometry with $b \approx 2a$ allows the intergrowth of a second layer of octahedra with the opposite tilt direction.

From crystal-chemical reasoning, the structure of $Hf_2B_{2-2\delta}Ir_{5+\delta}$ can thus be described in multiple ways. This raises the important question of which atomic interactions govern the formation of this compound and thus transcend the aforementioned mere geometrical perspective. This issue was tackled by applying a quantum chemical analysis of chemical bonding with position-space techniques, in particular the electron localizability approach.[80]

An analysis of the calculated electron density on application of the QTAIM reveals a relatively small volume of the Hf species in comparison with the iridium and boron species (Figure 4). Furthermore, the effective charge of hafnium, evaluated by integration over the electron density within the region formed by zero-flux surfaces in its gradient field around the nucleus of Hf, is unexpectedly large (+1.83). It is
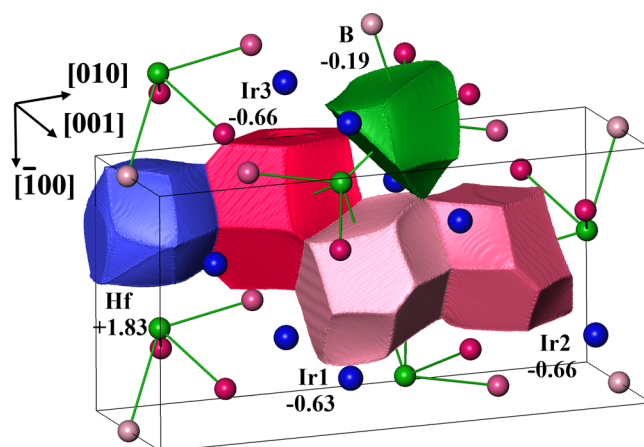

Figure 4. Shapes and effective charges of the QTAIM atoms in $Hf_2B_2Ir_5$.

essentially larger than even the charges of the filler atoms Ba (from +1.1 to +1.4[89]) and Sr (from +1.34 to +1.54[90,91]) in intermetallic clathrates. This fact allows us to assume strongly polar interactions of hafnium with its ligands. Along with this assumption, the shape of the Hf QTAIM species is convex and may resemble a sphere. The shapes of the QTAIM atoms of Ir and B are characterized by large close to planar faces, which are typical for covalent interactions. According to the difference in electronegativity, iridium and boron species are negatively charged, whereby the difference between the charges of the anions is much smaller in comparison with that of the hafnium cation (Figure 4).
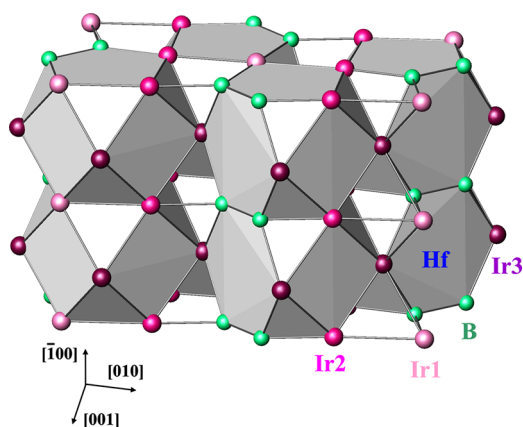
The distribution of the electron localizability indicator (ELI-D) in $Hf_2B_2Ir_5$ reveals strong maxima of the functional located on, or close to, the bond lines between the boron as well as between boron and iridium atoms (Figure 5). Moreover, the basin population of the B–B attractor in the dumbbell is around two electrons (2.18). The populations of the basins for boron–iridium bonds are formed by two or by three atomic contributions. For the four B–Ir bonds on each side of the dumbbell, 4.29 electrons are available (approximately one electron per bond). In all cases the contributions of boron and iridium to each basin are similar, indicating weakly polar covalent interactions.

These findings suggest that the boron dumbbell cannot be interpreted as an isolated structural unit and therefore—from a chemical bonding point of view—should be considered together with the attached iridium atoms as B_2Ir_8 fragments. Moreover, there are two- and three-center iridium–iridium interactions between the B_2Ir_8 units (Figure 5). The intersection of the atomic basins of hafnium with the bonding basins of the B–B, B–Ir, and Ir–Ir bonds shows a very small contribution of Hf to these bonding interactions. There are no bonding attractors in the vicinity of the hafnium nuclei, indicating a mostly ionic type of interaction in this region of the $Hf_2B_2Ir_5$ crystal structure and resembling strongly the bonding picture in intermetallic clathrates[89−91] or in recently found $MgSi_5$.[92] Another interesting feature of ELI-D appears in the vicinity of the Ir2 and Ir3 atoms within the cavity bearing hafnium atoms (the bonding basins are shown in gray and dark gray in Figure 5, bottom). Such a local ELI-D maximum reveals a donorlike interaction between the neighboring Ir2 or Ir3 and Hf atoms, being topologically similar to a bonding situation observed in the $Ba_8Au_{5.3}Ge_{40.7}$ intermetallic clathrate,
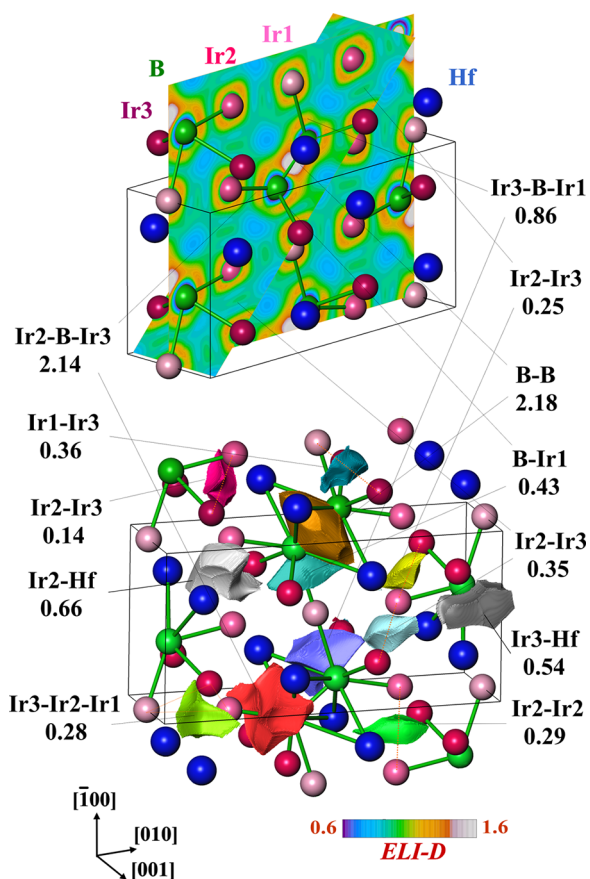
Figure 5. Electron localizability indicator ELI-D in $Hf_2B_2Ir_5$: (top) distribution of ELI-D in the (002) and (120) planes; (bottom) ELI-D basins and their populations (in e^-) for the two- and three-atom interactions.

where the ionic interaction of the filler atom Ba with the gold–germanium framework is additionally augmented by a covalent (dative) bonding between Ba and Au.[93] Surprisingly, an analysis of chemical bonding leads to the understanding of $Hf_2B_2Ir_5$ as a cage compound (Figure 6). Its crystal structure is formed by a three-dimensional anionic boron–iridium framework with cavities bearing the hafnium cations. The size of the cavities with 14 vertices is smaller than in the typical clathrates

with 15- to 24-atom cages but is similar to the those in $MgSi_5$[92] and $TmAlB_4$.[94]

3.2. Physical Properties. The temperature dependence of the magnetic susceptibility (corrected for the sum of diamagnetic increments) of $Hf_2B_{2-2\delta}Ir_{5+\delta}$ is depicted in Figure 7a. The susceptibility is on the same order of magnitude as those expected for a Pauli paramagnetic system. The fit of $\chi(T)$ to a modified Curie law ($C/T + \chi_0$) for $T > 100$ K resulted in
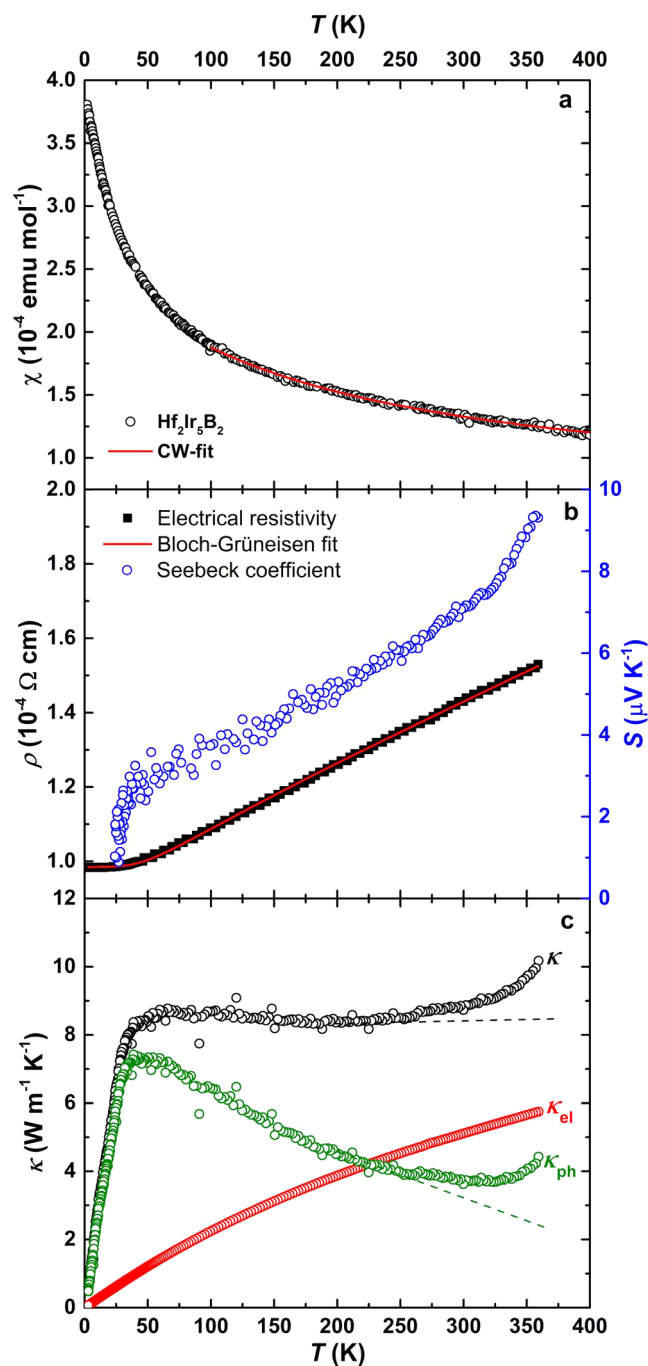
Figure 7. Low-temperature physical properties of $Hf_2B_{2-2\delta}Ir_{5+\delta}$: (a) magnetic susceptibility χ with the fit to a modified Curie law; (b) Seebeck coefficient S and electrical resistivity ρ with the fit to the Bloch–Grüneisen law; (c) thermal conductivity κ with electronic (κ_{el}) and phononic (κ_{ph}) contributions. κ and κ_{ph} are biased at higher temperatures due to radiation heat losses which follow roughly a $\propto T^3$ law (cf. dotted lines for expected behavior).

Figure 6. Cage-compound representation of $Hf_2B_2Ir_5$, as obtained from a quantum chemical analysis of chemical bonding.

$\chi_0 = +[6.3(2)] \times 10^{-5}$, in line with metallic behavior. An upturn in $\chi(T)$ for $T < 100$ K can be explained by paramagnetic impurities. No phase or superconducting transitions are detected down to 1.8 K.

As expected for a metal, the electrical resistivity of $Hf_2B_{2-2\delta}Ir_{5+\delta}$ increases with temperature in the entire temperature range studied (Figure 7b). $\rho(T)$ fits perfectly to the Bloch–Grüneisen (BG) equation:

$$\rho(T) = \rho_0 + A\left(\frac{T}{\Theta_R}\right)^n \int_0^{\Theta_R/T} \frac{x^n}{(e^x-1)(1-e^{-x})}\,dx \tag{1}$$

with $n = 5$ (implying $\rho(T)$ to be mainly due to electron–phonon scattering), the residual resistivity $\rho_0 = 0.99(1)$ $\mu\Omega$ m, the phonon contribution coefficient $A = 0.018(1)$ $\mu\Omega$ m, and the Debye temperature $\Theta_R = 285(2)$ K. However, heat capacity measurements are required to shed more light on the lattice thermal properties. $Hf_2B_{2-2\delta}Ir_{5+\delta}$ displays only a moderate hardness of HV(0.1) = 13(1) GPa (see the Supporting Information).

The Seebeck coefficient $S(T)$ is small and varies linearly with temperature (Figure 7b), which is again typical for metallic systems.[95] The positive values of the Seebeck coefficient indicate predominant p-type charge carriers.

The Hall effect measurements indicated a charge carrier density of $\sim 10^{28}$ m^{-3} for $Hf_2B_{2-2\delta}Ir_{5+\delta}$, which is on the same order of magnitude as for a good metal. Additionally, it confirmed the holelike electrical conductivity, in agreement with the result observed in $S(T)$.

The thermal conductivity $\kappa(T)$ for $Hf_2B_{2-2\delta}Ir_{5+\delta}$ is depicted in Figure 7c. It increases almost linearly with temperature, reaches its maximum value of ~ 9 W m^{-1} K^{-1} at around 70 K, and remains almost temperature independent up to 300 K. Normally, a good metallic system is characterized by a well-pronounced maximum in $\kappa(T)$ centered at $\sim 100-200$ K.[96] Its absence indicates a higher concentration of point defects.[97] This finding is in good agreement with the performed electrical resistivity measurements.

We calculated the electronic part of $\kappa(T)$ by applying the Wiedemann–Franz law $\kappa_{el} = LT\rho^{-1}$, with the Lorenz number $L = 2.44 \times 10^{-8}$ W Ω K^{-2}. As one can see from Figure 7c, the lattice thermal conductivity κ_{ph} dominates $\kappa(T)$ below 200 K, while for a higher temperature range $\kappa(T)$ is mainly due to κ_{el}.

3.3. Electronic Structure. The total and atomically resolved electronic densities of states (DOSs) for $Hf_2B_2Ir_5$ are presented in Figure 8. The calculations resulted in 5.8 states eV^{-1} fu^{-1} at the Fermi level E_F, confirming the metallic electronic transport properties of the studied boride. Interestingly, the Fermi level is situated at a local maximum of the DOS, suggesting possible electronic or structural instabilities.

The electronic DOS of $Hf_2B_2Ir_5$ consists of two energy regions: low-lying states between -11 and -7.5 eV and a broad valence band extending from -7.5 eV to E_F. The low-energy region is mainly due to B(2s) states, while the valence band is dominated by Ir(5d) states with an admixture of Hf(5d) and B(2p) electrons (Figure 8b). Also, the Ir(5d) states are contributing ca. 65% at the Fermi level.

4. SUMMARY AND CONCLUSIONS

The metal-rich refractory intermetallic borides $Hf_2B_{2-2\delta}Ir_{5+\delta}$, $Hf_{2-x}B_{2-2\delta}Zr_xIr_{5+\delta}$, and $Zr_2B_{2-2\delta}Ir_{5+\delta}$ ($x \approx 0.5$, $\delta \approx 0.05$) have
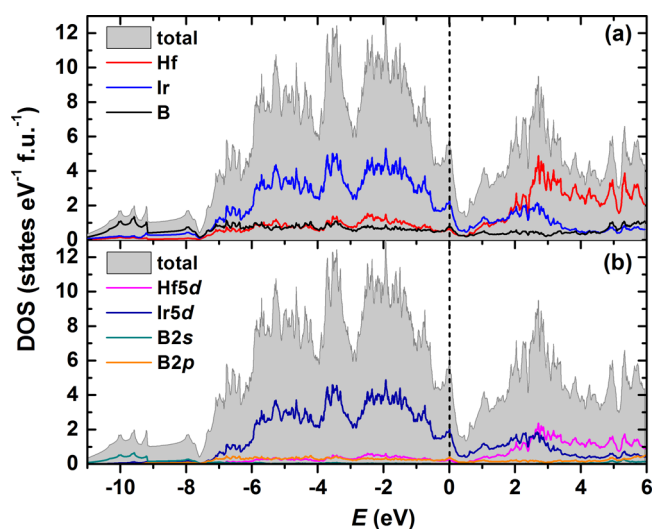
Figure 8. Calculated electronic densities of states (DOSs) for $Hf_2B_2Ir_5$ with (a) atomic contributions and (b) orbital projected DOS. The Fermi level is set to 0 eV.

been synthesized. They crystallize with a new orthorhombic structure type, where boron atoms are found in a dumbbell-like arrangement. Approximately 5% of the boron dumbbells are randomly substituted by single iridium atoms. From a crystal-chemical point of view, these dumbbells reside in rhombic prismatic [Ir$_8$] slabs along [001] which can be decomposed into face-sharing trigonal [Ir$_6$] prisms hosting the boron atoms. Such boron-centered metal prisms represent a typical structural unit of the hexagonal AlB$_2$ type. As observed for borides with a high metal to boron ratio, the boron-containing structural units are integrated into a metal matrix which in $Hf_2B_2Ir_5$ is composed of face-sharing Ir-centered [Hf$_4$Ir$_4$] cuboids resembling the elemental α-Fe structure.

Unexpectedly, an analysis of chemical bonding interactions yields a quite different picture of $Hf_2B_{2-2\delta}Ir_{5+\delta}$. Apart from the multiple B$_2$-by-Ir substitutions, this material is a cage compound with a three-dimensional anionic boron–iridium framework with cavities bearing the hafnium cations. More-over, this bonding situation strikingly resembles that in the large family of Ge-based inorganic clathrates in terms of all basic aspects: covalent bonds in the framework, ionic framework–guest atom interactions, and two-center covalent bonds between the host and the transition-metal component of the framework. The position-space chemical bonding analysis elucidated hitherto unknown similarities between such apparently unrelated intermetallic compounds.

$Hf_2B_{2-2\delta}Ir_{5+\delta}$ is a Pauli paramagnet with a low DOS at the Fermi level. Metallic behavior was further confirmed by the measurements of electrical and thermal transport properties and was corroborated by electronic structure calculations.

■ ASSOCIATED CONTENT

ⓢ Supporting Information

The Supporting Information is available free of charge at https://pubs.acs.org/doi/10.1021/acs.inorgchem.0c02073.

Selected interatomic distances, 3D crystal structure representations, and results from micro hardness measurements (PDF)

Accession Codes

CCDC 2012569 contains the supplementary crystallographic data for this paper. These data can be obtained free of charge via www.ccdc.cam.ac.uk/data_request/cif, or by emailing data_request@ccdc.cam.ac.uk, or by contacting The Cambridge Crystallographic Data Centre, 12 Union Road, Cambridge CB2 1EZ, UK; fax: +44 1223 336033.

■ AUTHOR INFORMATION

Corresponding Author

    Andreas Leithe-Jasper − *Max-Planck-Institut für Chemische Physik fester Stoffe, 01187 Dresden, Germany;* ⊙ orcid.org/0000-0001-7688-4365; Email: jasper@cpfs.mpg.de

Authors

    Olga Sichevych − *Max-Planck-Institut für Chemische Physik fester Stoffe, 01187 Dresden, Germany*

    Sever Flipo − *Max-Planck-Institut für Chemische Physik fester Stoffe, 01187 Dresden, Germany; Institut für Experimentelle Physik, TU Bergakademie Freiberg, 09599 Freiberg, Germany*

    Alim Ormeci − *Max-Planck-Institut für Chemische Physik fester Stoffe, 01187 Dresden, Germany*

    Matej Bobnar − *Max-Planck-Institut für Chemische Physik fester Stoffe, 01187 Dresden, Germany*

    Lev Akselrud − *Max-Planck-Institut für Chemische Physik fester Stoffe, 01187 Dresden, Germany*

    Yurii Prots − *Max-Planck-Institut für Chemische Physik fester Stoffe, 01187 Dresden, Germany*

    Ulrich Burkhardt − *Max-Planck-Institut für Chemische Physik fester Stoffe, 01187 Dresden, Germany*

    Roman Gumeniuk − *Max-Planck-Institut für Chemische Physik fester Stoffe, 01187 Dresden, Germany; Institut für Experimentelle Physik, TU Bergakademie Freiberg, 09599 Freiberg, Germany*

    Yuri Grin − *Max-Planck-Institut für Chemische Physik fester Stoffe, 01187 Dresden, Germany;* ⊙ orcid.org/0000-0003-3891-9584

Complete contact information is available at:
https://pubs.acs.org/10.1021/acs.inorgchem.0c02073

Notes

The authors declare no competing financial interest.

■ DEDICATION

The authors dedicate this Article to Prof. Peter Franz Rogl on the occasion of his 75th birthday.

■ REFERENCES

(1) Kuz'ma, Yu. B. *Crystal chemistry of borides*; Vyshcha Shkola: Lviv, 1983.

(2) Albert, B.; Hillebrecht, H. Boron: Elementary Challenge for Experimenters and Theoreticians. *Angew. Chem., Int. Ed.* **2009**, *48*, 8640−8668.

(3) Kiessling, R.; Hagdahl, L.; Sillen, L. G.; Rottenberg, M. The Borides of Some Transition Elements. *Acta Chem. Scand.* **1950**, *4*, 209−227.

(4) Rogl, P. Existence and Crystal Chemistry of Borides. In *Inorganic Reactions and Methods*; Zuckerman, J. J., Ed.; VCH: 1991; Vol. *13* (6), p 85 and references therein.

(5) Fokwa, B. P.; Borides, T. Solid state chemistry. In *Encyclopedia of Inorganic and Bioinorganic Chemistry*; Scott, R. A., Ed.; Wiley: 2014.

(6) Matkovich, V. *Boron and Refractory Borides*; Springer: Berlin, 1977.

(7) Akopov, G.; Yeung, M. T.; Kaner, R. B. Rediscovering the Crystal Chemistry of Borides. *Adv. Mater.* **2017**, *29*, 1604506.

(8) Gao, F. M.; Gao, L. H. Microscopic models of hardness. *J. Superhard Mater.* **2010**, *32*, 148−166.

(9) Schwarzkopf, P.; Kieffer, R.; Leszynski, W.; Benesovsky, K. *Refractory Hard Metals; Borides, Carbides, Nitrides, and Silicides*; Macmillan: New York, 1953.

(10) Takagi, K.; Komai, M.; Watanabe, T.; Kondo, Y. Effect of Ni on the mechanical properties of Fe, Mo Boride hard alloys. *Int. J. Powder Metallurgy* **1987**, *23*, 157−161.

(11) Ettmayer, P. Hardmetals and cermets. *Annu. Rev. Mater. Sci.* **1989**, *19*, 145−164.

(12) Takagi, K.; Yamasaki, Y.; Komai, M. High-Strength Boride Base Hard Materials. *J. Solid State Chem.* **1997**, *133*, 243−248.

(13) Lark, A.; Du, J.; Chandra, K. S. R. Material design and processing of a new class of titanium boride cermets with tough metallic phases and mechanical properties. *J. Mater. Res.* **2018**, *33*, 4296−4306.

(14) Zimmerman, C. Boriding (Boronizing) of Metals. In *ASM Handbook*; Dossett, J. L., Totten, G. E., Eds.; ASM International: 2013; Vol. *4A*, p 709.

(15) Fahrenholtz, W. G.; Hilmas, G. E.; Talmy, I. G.; Zaykoski, J. A. Refractory Diborides of Zirconium and Hafnium. *J. Am. Ceram. Soc.* **2007**, *90*, 1347−1364.

(16) Corral, E. L.; Loehman, R. E. Ultra-High-Temperature Ceramic Coatings for Oxidation Protection of Carbon−Carbon Composites. *J. Am. Ceram. Soc.* **2008**, *91*, 1495−1502.

(17) Kaner, R. B.; Gilman, J. J.; Tolbert, S. H. Designing Superhard Materials. *Science* **2005**, *308*, 1268−1269.

(18) Chung, H. Y.; Weinberger, M. B.; Levine, J. B.; Kavner, A.; Jang, J. M.; Tolbert, S. H.; Kaner, R. B. Synthesis of ultra-incompressible superhard rhenium diboride at ambient pressure. *Science* **2007**, *316*, 436−439.

(19) Cumberland, R. W.; Weinberger, M. B.; Gilman, J. J.; Clark, S. M.; Tolbert, S. H.; Kaner, R. B. Osmium Diboride, An Ultra-Incompressible, Hard Material. *J. Am. Chem. Soc.* **2005**, *127*, 7264−7265.

(20) Levine, J. B.; Tolbert, S. H.; Kaner, R. B. Advancements in the Search for Superhard Ultra-Incompressible Metal Borides. *Adv. Funct. Mater.* **2009**, *19*, 3519−3533.

(21) Lazar, P.; Chen, X. Q.; Podloucky, R. First-principles modeling of hardness in transition-metal diborides. *Phys. Rev. B: Condens. Matter Mater. Phys.* **2009**, *80*, No. 012103.

(22) Zeiringer, I.; Rogl, P.; Grytsiv, A.; Polt, J.; Bauer, E.; Giester, G. Crystal Structure of $W_{1−x}B_3$ and Phase Equilibria in the Boron-Rich Part of the Systems Mo-Rh-B and W-{Ru,Os,Rh,Ir,Ni,Pd,Pt}-B. *J. Phase Equilib. Diffus.* **2014**, *35*, 384−394.

(23) Akopov, G.; Pangilinan, L. E.; Mohammadi, R.; Kaner, R. B. Perspective: Superhard metal borides: A look forward. *APL Mater.* **2018**, *6*, No. 070901.

(24) Wang, N.; Fu, Z.; Legut, D.; Wie, B.; Germann, T. C.; Zhang, R. Designing ultrastrong 5d transition metal diborides with excellent stability for harsh service environments. *Phys. Chem. Chem. Phys.* **2019**, *21*, 16095−16107.

(25) Zhang, Z.; Tehrani, A. M.; Brgoch, J. Tailoring the Mechanical Properties of Earth-Abundant Transition Metal Borides via Bonding Optimization. *J. Phys. Chem. C* **2020**, *124*, 4430−4437.

(26) Glaser, F. W.; Moskowitz, D.; Post, B. Study of Some Binary Hafnium Compounds. *Trans. AIME* **1953**, *197*, 1119−1120.

(27) Henschel, A.; Binnewies, M.; Schmidt, M.; Borrmann, H.; Grin, Yu. Crucible-Free Preparation of Transition-Metal Borides: HfB_2. *Chem. - Eur. J.* **2017**, *23*, 15869−15873.

(28) Guo, H.; Buiron, L.; Kooyman, T.; Sciora, P. Optimized control rod designs for Generation-IV fast reactors using alternative absorbers and moderators. *Ann. Nucl. Energy* **2019**, *132*, 713−722.

(29) Rubio, V.; Ramanujam, P.; Binner, J. Ultra-high temperature ceramic composite. *Adv. Appl. Ceram.* **2018**, *117*, s56−s61.

(30) Silvestroni, L.; Gilli, N.; Migliori, A.; Sciti, D.; Watts, J.; Hilmas, G. E.; Fahrenholtz, W. G. A simple route to fabricate strong boride hierarchical composites for use at ultra-high temperature. *Composites, Part B* **2020**, *183*, 107618.

(31) Buddery, J. H.; Welch, A. J. E. Borides and Silicides of the Platinum Metals. *Nature* **1951**, *167*, 362.

(32) Aronsson, B.; Stenberg, E.; Aselius, J.; Refn, S.; Westin, G. Borides of Rhenium and the Platinum Metals. The Crystal Structure of Re_7B_3, ReB_3, Rh_7B_3, $RhB_{\sim1.1}$, $IrB_{\sim1.1}$ and PtB. *Acta Chem. Scand.* **1960**, *14*, 733−741.

(33) Aronsson, B.; Leden, I.; Sunner, S.; Hatanaka, A.; Munch-Petersen, J. The Crystal Structure of RuB_2, OsB_2, and $IrB_{1.35}$ and Some General Comments on the Crystal Chemistry of Borides in the Composition Range MeB − MeB_3. *Acta Chem. Scand.* **1963**, *17*, 2036−2050.

(34) Rogl, P.; Benesovsky, F.; Nowotny, H. Complex borides with platinum metals. *Monatsh. Chem.* **1972**, *103*, 965−989.

(35) Ipser, H.; Rogl, P. Constitution diagrams of the binary systems Pd-B and Ir-B. *J. Less-Common Met.* **1981**, *82*, 363.

(36) Rogl, P.; Nowotny, H.; Benesovsky, F. A contribution to the crystal structures of the iridium borides. *Monatsh. Chem.* **1971**, *102*, 678−686.

(37) Zeiringer, I.; Cheng, X.; Chen, X.-Q.; Bauer, E.; Giester, G.; Rogl, P. Crystal structures and constitution of the binary system iridium-boron. *Sci. China Mater.* **2015**, *58*, 649−668.

(38) Rau, J. V.; Latini, A. New Hard and Superhard Materials: $RhB_{1.1}$ and $IrB_{1.35}$. *Chem. Mater.* **2009**, *21*, 1407−1409.

(39) Zhao, W. J.; Wang, J. X. Structural, mechanical, and electronic properties of TaB_2, TaB, IrB_2, and IrB: first-principle calculations. *J. Solid State Chem.* **2009**, *182*, 2880−2886.

(40) Petermüller, B.; Neun, C.; Wurst, K.; Boyarjagal, L.; Zimmer, D.; Morgenroth, W.; Avalos-Borja, M.; Becerril-Juarez, I. G.; Mühlbauer, M. J.; Winkler, B.; Huppertz, H. High-Pressure Synthesis of β-Ir_4B_5 and Determination of the Compressibility of Various Iridium Borides. *Inorg. Chem.* **2018**, *57*, 10341−10351.

(41) Kuz'ma, Y. B.; Bilonizhko, N.S.; Mykhalenko, S.I.; Stepanchikova, G.F.; Chaban, N.F. The interaction of transition and rare earth metals with boron. *J. Less-Common Met.* **1979**, *67*, 51−57.

(42) Villars, P. *Pearson's Handbook: Crystallographic Data for intermetallic phases*; ASM International: 1997.

(43) Scheifers, J. P.; Zhang, Y.; Fokwa, B. P. T. Boron: Enabling Exciting Metal-Rich Structures and Magnetic Properties. *Acc. Chem. Res.* **2017**, *50*, 2317−2325.

(44) Kuzma, Yu. B.; Chaban, N. F. Binary and Ternary Systems containing boron. *Metallurgia publishers*, Moscow, **1990**. (in Russian)

(45) Vandenberg, J. M.; Matthias, B. T.; Corenzwit, E.; Barz, H. Superconductivity of some binary and ternary transition-metal borides. *Mater. Res. Bull.* **1975**, *10*, 889−894.

(46) Johnston, D. C. Superconductivity in a new ternary structure class of boride compounds. *Solid State Commun.* **1977**, *24*, 699−702.

(47) Matthias, B. T.; Corenzwit, E.; Vandenberg, J. M.; Barz, H. E. High superconducting transition temperatures of new rare earth ternary borides. *Proc. Natl. Acad. Sci. U. S. A.* **1977**, *74*, 1334−1335.

(48) Müller, K. H.; Narozhnyi, V. N. Interaction of superconductivity and magnetism in borocarbide superconductors. *Rep. Prog. Phys.* **2001**, *64*, 943−1008.

(49) Togano, K.; Badica, P.; Nakamori, Y.; Orimo, S.; Takeya, H.; Hirata, K. Superconductivity in the Metal Rich Li-Pd-B Ternary Boride. *Phys. Rev. Lett.* **2004**, *93*, 247004.

(50) Buzea, C.; Yamashita, T. Review of the superconducting properties of MgB_2. *Supercond. Sci. Technol.* **2001**, *14*, R115.

(51) Wolowiec, C.T.; White, B.D.; Maple, M.B. Conventional magnetic superconductors. *Phys. C* **2015**, *514*, 113−129.

(52) Fokwa, B. P. T. Transition-Metal-Rich Borides − Fascinating Crystal Structures and Magnetic Properties. *Eur. J. Inorg. Chem.* **2010**, *2010*, 3075−3092.

(53) Yamabe, Y.; Koizumi, Y.; Murakami, H.; Ro, Y.; Maruko, T.; Harada, H. Development of Ir-base refractory superalloys. *Scr. Mater.* **1996**, *35*, 211−215.

(54) Cornish, L. A.; Fischer, B.; Völkl, R. Development of platinum-group-metal superalloys for high-temperature use. *MRS Bull.* **2003**, *28*, 632−638.

(55) Wu, J.; Zhang, B.; Zhan, Y. Ab initio investigation into the structure and properties of Ir−Zr intermetallics for high-temperature structural applications. *Comput. Mater. Sci.* **2017**, *131*, 146−159.

(56) Idbenali, M.; Servant, C.; Feddaoui, M. Thermodynamic assessment of Hafnium Iridium binary system. *Metall. Res. Technol.* **2018**, *115*, 503.

(57) Baklanova, N. I.; Lozanov, V. V.; Titov, A. T. The first evidence of the high oxidation resistance of the novel ternary tantalum-iridium-boron phase. *Corros. Sci.* **2019**, *160*, 108178.

(58) Zheng, Q.; Kohout, M.; Gumeniuk, R.; Abramchuk, N.; Borrmann, H.; Prots, Yu.; Burkhardt, U.; Schnelle, W.; Akselrud, L.; Gu, H.; Leithe-Jasper, A.; Grin, Yu. $TM_7TM'_6B_6$ (TM = Ta, Nb; TM' = Ru, Rh, Ir): New Compounds with $[B_6]$ Ring Polyanions. *Inorg. Chem.* **2012**, *51*, 7472−7483.

(59) Wu, W.-P.; Chen, Z.-F. Iridium Coating: Processes, Properties and Application. *Johnson Matthey Technol. Rev.* **2017**, *61*, 16−28.

(60) Duvall, D. S.; Owczarski, W. A.; Paulonis, D. F. Transient Liquid Phase Bonding: A New Method for Joining Heat Resistant Alloys. *Welding J.* **1974**, *53*, 203−214.

(61) Zhou, Y.; Gale, W. F.; North, T. H. Modelling of transient liquid phase bonding. *Int. Mater. Rev.* **1995**, *40*, 181−196.

(62) Gale, W. F.; Butts, D. A. Transient liquid phase bonding. *Sci. Technol. Weld. Joining* **2004**, *9*, 283−300.

(63) Sha, J. B.; Yamabe-Mitarai, Y. Ir−Hf−Zr ternary refractory superalloys for ultra-high temperatures — Phase and microstructural constitution. *Intermetallics* **2013**, *41*, 1−9.

(64) Levy, O.; Hart, G. L. W.; Curtarolo, S. Hafnium binary alloys from experiments and first principles. *Acta Mater.* **2010**, *58*, 2887−2897.

(65) Lozanov, V. V.; Baklanova, N. I.; Bulina, N. V.; Titov, A. T. New Ablation-Resistant Material Candidate for Hypersonic Applications: Synthesis, Composition, and Oxidation Resistance of $HfIr_3$-Based Solid Solution. *ACS Appl. Mater. Interfaces* **2018**, *10*, 13062−13072.

(66) Steuer, S.; Singer, R. F. Suppression of Boride Formation in Transient Liquid Phase Bonding of Pairings of Parent Superalloy Materials with Different Compositions and Grain Structures and Resulting Mechanical Properties. *Metall. Mater. Trans. A* **2014**, *45*, 3545−3553.

(67) Hu, X. B.; Sheng, N. C.; Zhu, Y. M.; Nie, J. F.; Liu, J. D.; Sun, X. F.; Ma, X. L. Atomic-Scale Investigation of the Borides Precipitated in a Transient Liquid Phase-Bonded Ni-Based Superalloy. *Metall. Mater. Trans. A* **2020**, *51*, 1689−1698.

(68) Rogl, P.; Nowotny, H. Study of the (Sc, Zr, Hf)-(Rh, Ir)-B systems. *J. Less-Common Met.* **1979**, *67*, 41−50.

(69) Rogl, P. The crystal structure of $ZrIr_3B_{\sim4}$. *Acta Crystallogr., Sect. B: Struct. Crystallogr. Cryst. Chem.* **1978**, *34*, 721−724.

(70) Hermus, M.; Fokwa, B. P. T. Zr_2Ir_6B with an eightfold superstructure of the cubic perovskite-like boride $ZrIr_3B_{0.5}$: Synthesis, crystal structure and bonding analysis. *J. Solid State Chem.* **2010**, *183*, 784−788.

(71) Kuz'ma, Y. B.; Yarmolyuk, Y. P. Crystal structure of the compound $Ti_3Co_5B_2$. *J. Struct. Chem.* **1971**, *12*, 422−424.

(72) *WinXPow*; STOE and Cie: Darmstadt, Germany, 2003.

(73) Eikenberry, E. F.; Brönnimann, C.; Hülsen, G.; Toyokawa, H.; Horisberger, R.; Schmitt, B.; Schulze-Briese, C.; Tomizaki, T. PILATUS: a two-dimensional X-ray detector for macromolecular

crystallography. *Nucl. Instrum. Methods Phys. Res., Sect. A* **2003**, *501*, 260−266.

(74) Kieffer, J.; Karkoulis, D. PyFAI, a versatile library for azimuthal regrouping. *J. Phys.: Conf. Ser.* **2013**, *425*, 202012.

(75) Akselrud, L.; Grin, Yu. WinCSD: software package for crystallographic calculations (Version 4). *J. Appl. Crystallogr.* **2014**, *47*, 803−805.

(76) Koepernik, K.; Eschrig, H. Full-potential nonorthogonal local-orbital minimum-basis band-structure scheme. *Phys. Rev. B: Condens. Matter Mater. Phys.* **1999**, *59*, 1743−1757.

(77) Perdew, J. P.; Wang, Y. Accurate and simple analytic representation of the electron-gas correlation energy. *Phys. Rev. B: Condens. Matter Mater. Phys.* **1992**, *45*, 13244−13249.

(78) Bader, R. F. W. *Atoms in Molecules: A Quantum Theory*; Oxford University Press and Clarendon Press: 1994.

(79) Kohout, M. A measure of electron localizability. *Int. J. Quantum Chem.* **2004**, *97*, 651.

(80) Kohout, M.; Wagner, F. R.; Grin, Yu. Atomic shells from the electron localizability in momentum space. *Int. J. Quantum Chem.* **2006**, *106*, 1499.

(81) Kohout, M. Bonding indicators from electron pair density functionals. *Faraday Discuss.* **2007**, *135*, 43.

(82) Ormeci, A.; Rosner, H.; Wagner, F. R.; Kohout, M.; Grin, Yu. Electron Localization Function in Full-Potential Representation for Crystalline Materials. *J. Phys. Chem. A* **2006**, *110*, 1100.

(83) Kohout, M. *DGrid, ver. 4.6−5.1*, 2011−2019.

(84) Emsley, J. *The Elements*; Oxford University Press: 1998.

(85) Kuz'ma, Yu. B.; Krypyakevich, P. I.; Bilonizhko, N. S. Crystal structure of $CeCo_3B_2$ and analogous compounds. *Dopov. Akad. Nauk Ukr. RSR Ser. A* **1969**, *31*, 939−941.

(86) Rogl, P. Existence and Crystal Chemistry of Borides. In *Inorganic Reactions and Methods*; Zuckerman, J. J., Hagen, A. P., Eds.; VCH: 2007.

(87) Ade, M.; Hillebrecht, H. Ternary Borides Cr_2AlB_2, Cr_3AlB_4, and Cr_4AlB_6: The First Members of the Series $(CrB_2)_nCrAl$ with $n =$ 1, 2, 3 and a Unifying Concept for Ternary Borides as MAB-Phases. *Inorg. Chem.* **2015**, *54*, 6122−6135.

(88) Gladyshevskii, E. I.; Fedorov, T. F.; Kuz'ma, Yu. B.; Skolozdra, R. V.; Hladyshevskii, E. I. Isothermal section of the molybdenum-iron-boron system. *Poroshkovaya Metall.* **1966**, *5*, 305−309.

(89) Ormeci, A.; Grin, Yu. Coexistence of ionic and covalent atomic interactions (bonding inhomogeneity) and thermoelectric properties of intermetallic clathrates. *J. Thermoelectricity* **2015**, *6*, 16.

(90) Hübner, J.-M.; Prots, Yu.; Schnelle, W.; Bobnar, M.; König, M.; Baitinger, M.; Simon, P.; Carrillo-Cabrera, W.; Ormeci, A.; Svanidze, E.; Grin, Yu.; Schwarz, U. In-Cage Interactions in the Clathrate Superconductor Sr_8Si_{46}. *Chem. - Eur. J.* **2020**, *26*, 830−838.

(91) Roudebush, J. H.; Tsujii, N.; Hurtando, A.; Hope, H.; Grin, Yu.; Kauzlarich, S. M. Phase range of the type-I clathrate $Sr_8Al_{(x)}Si_{(46-x)}$ and crystal structure of $Sr_8Al_{10}Si_{36}$. *Inorg. Chem.* **2012**, *51*, 4161−4169.

(92) Hübner, J.-M.; Carrillo-Cabrera, W.; Prots, Yu.; Bobnar, M.; Schwarz, U.; Grin, Yu. Unconventional Metal−Framework Interaction in $MgSi_5$. *Angew. Chem., Int. Ed.* **2019**, *58*, 12914−12918.

(93) Zhang, H.; Borrmann, H.; Oeschler, N.; Candolfi, C.; Schnelle, W.; Schmidt, M.; Burkhardt, U.; Baitinger, M.; Zhao, J.-T.; Grin, Yu. Atomic Interactions in the p-Type Clathrate I $Ba_8Au_{5.3}Ge_{40.7}$. *Inorg. Chem.* **2011**, *50*, 1250−1257.

(94) Mori, T.; Borrmann, H.; Okada, S.; Kudou, K.; Leithe-Jasper, A.; Burkhardt, U.; Grin, Yu. Crystal structure, chemical bonding, electrical transport, and magnetic behavior of $TmAlB_4$. *Phys. Rev. B: Condens. Matter Mater. Phys.* **2007**, *76*, No. 064404.

(95) Blatt, F. J.; Schroeder, P. A.; Foiles, C. L.; Greig, D. *Thermoelectric power of metals*; Plenum Press: New York, 1976.

(96) Groß, R.; Marx, A. *Festkörperphysik*, 3rd ed.; De Gruyter: Berlin/Boston, 2018.

(97) Tritt, T. M. *Thermal conductivity: theory, properties, and application*; Springer Science & Business Media: Berlin, 2005.

(98) Alekseeva, A. M.; Abakumov, A. M.; Chizhov, P. S.; Leithe-Jasper, A.; Schnelle, W.; Prots, Yu.; Hadermann, J.; Antipov, E. V.; Grin, Yu. Ternary Magnesium Rhodium Boride $Mg_2Rh_{1-x}B_{6+2x}$ with a Modified Y_2RhB_6-Type Crystal Structure. *Inorg. Chem.* **2007**, *46*, 7378−7386.

(99) Bérar, J.-F.; Lellan, P. E.s.d.'s and estimated probable errors obtained in Rietveld refinements with local correlations. *J. Appl. Crystallogr.* **1991**, *24*, 1−5.